Progress In Electromagnetics Research, Vol. 128, 457–477, 2012

A STUDY ON MILLIMETER-WAVE IMAGING OF CONCEALED OBJECTS: APPLICATION USING BACK-PROJECTION ALGORITHM

S. Demirci[1, *], H. Cetinkaya[2], E. Yigit[3], C. Ozdemir[1, 4], and A. Vertiy[2]

[1]Department of Electrical-Electronics Engineering, Mersin University, Ciftlikkoy, Mersin 33343, Turkey

[2]Material Institute, International Laboratory for High Tech. (ILHT), TUBITAK MRC, Gebze, Kocaeli, Turkey

[3]Vocational School of Technical Sciences, Mersin University, Ciftlikkoy, Mersin 33343, Turkey

[4]Department of Electrical-Electronics Engineering, Zirve University, Kızılhisar, Gaziantep 27260, Turkey

Abstract—Millimeter-wave (MMW) imaging is a powerful tool for the detection of objects concealed under clothing. Several factors including different kinds of objects, variety of covering materials and their thickness, accurate imaging of near-field scattered data affect the success of detection. To practice with such considerations, this paper presents the two-dimensional (2D) images of different targets hidden under various fabric sheets. The W-band inverse synthetic aperture radar (ISAR) data of various target-covering situations are acquired and imaged by applying both the focusing operator based inversion algorithm and the spherical back-projection algorithm. Results of these algorithms are demonstrated and compared to each other to assess the performance of the MMW imaging in detecting the concealed objects of both metallic and dielectric types.

1. INTRODUCTION

Recently, there has been an increasing trend towards the use of the millimeter-wave (MMW) based imaging in various detection applications. This is mainly due to two factors: firstly, the radiation

Received 2 May 2012, Accepted 27 May 2012, Scheduled 5 June 2012

* Corresponding author: Sevket Demirci (sdemirci@mersin.edu.tr).

in the MMW band (30–300 GHz) is nonionizing and safe to use and secondly it is able to penetrate through most dielectric materials as well as poor weather conditions such as smoke and fog [1]. High resolution imaging due to short wavelength usage can also be easily achieved in the MMW band. With these abilities, MMW imaging has been used in a variety of applications including target surveillance and precision target imaging for military purposes [2]; safe aircraft landing [3], highway traffic monitoring in fog [4], remote sensing for civil applications [5] and concealed threat object detection for security concerns [6]. There are also some reported examples in the non-destructive testing field where the dielectric material defects are detected with the good penetration ability of MMW signals [7, 8].

Among the MMW imaging practices, the detection of threat objects concealed under clothing has been one of the most studied applications as a result of increasing demand for defeating terrorism. For this purpose,various researchers have demonstrated both passive and active imaging systems [9–27]. Passive imaging systems are based on the detection of natural radiation from the targets and reflection from the environment [9–12] and hence mostly limited to outdoor missions. Besides, the lack of range information in the provided two-dimensional (2D) images puts an additional limit on the detection problem. On the other hand, active imaging systems [13–27] exploit various radar systems giving rise to indoor operation as well as sharp range resolving ability. Hence, the position and shape of the concealed objects can be attained from the produced three-dimensional (3D) images. The active imaging, though, faces some challenges in fulfilling the vital requirements such as fast scanning of the whole body from all aspects and accurate imaging of the acquired near-field data. For this reason, various studies have been focused on the different scanning set-ups along with the consideration of the appropriate near-field reconstruction algorithms [21–27]. In [21], Sheen et al., originally adapted planar scanning aperture and 3D range migration algorithm (RMA) for imaging the human body. In a more recent work, this proposed scanning geometry and imaging was followed to investigate the effects of the system parameters such as different clothing materials, target orientations, aperture sizes and samplings on the imaging performance [22]. In [23] and [24], the detection problem was investigated through 2D cylindrical scanning geometry which is the common practice for imaging the body from all aspects. Thanks to availability of its cylindrical formulation and also its computational efficiency, the RMA has been effectively used in these studies [28]. Although RMA seems to be the conventional imaging technique, it comes with a difficult implementation for the bistatic

configuration [29] of which usage may be favorable to increase the detection capabilities. As an alternative, the back-projection algorithm that is directly applicable to any data collection geometry has been recently employed in a few studies of the concealed object detection problem [25–27]. In these studies, both the monostatic [25] and the bistatic [26] imaging performances were investigated for the cylindrical reconstruction surface.

In this paper, we investigate the performance of MMW imaging in detecting small ($\sim$ 1 cm^3), metallic and dielectric targets as a contribution to the above-mentioned developments in concealed object detection. The detection performance for a real handgun target is also restudied for comparison purposes and to reveal the importance of target's physical properties on detection. The W-band, measured images of these targets are demonstrated for the 2D inverse synthetic aperture radar (ISAR) data collection geometry. Various factors; including radar system parameters, reconstruction of the target's reflectivity function and variety of covering materials and their thickness are addressed to comprehend their effects on an effective detection. Two different imaging algorithms namely; the focusing operator based [30] and the back-projection [31, 32] are employed to focus the wide-angle backscattering data. Issues regarding sampling requirements and resolution prediction for a full-aperture, i.e., 360° collection geometry are also reviewed and presented to maintain the completeness.

The paper is organized as follows: Next section provides the theoretical formulation of the focusing operator based imaging and the back-projection based imaging algorithms. The critical parameters such as sampling, resolution and calibration are also covered in this section. In the third section, the experimental set-up is introduced and the constructed near-field MMW images of different concealed objects are presented. Concluding remarks and the assessment of this study are given in the final section.

2. 2D MONOSTATIC MMW IMAGING SYSTEM

Although a feasible concealed object detection approach mostly necessities 3D imaging arrangement, our main focus in this study is to investigate the detection capabilities of the MMW imaging approach through the processing of 2D monostatic backscattering data from concealed objects of different types. The following formulation therefore assumes the one-dimensional (1D) circular receiving aperture case of the full cylindrical scanning geometry (see Fig. 1). As shown from the figure, a transceiver antenna that moves on a target-centered

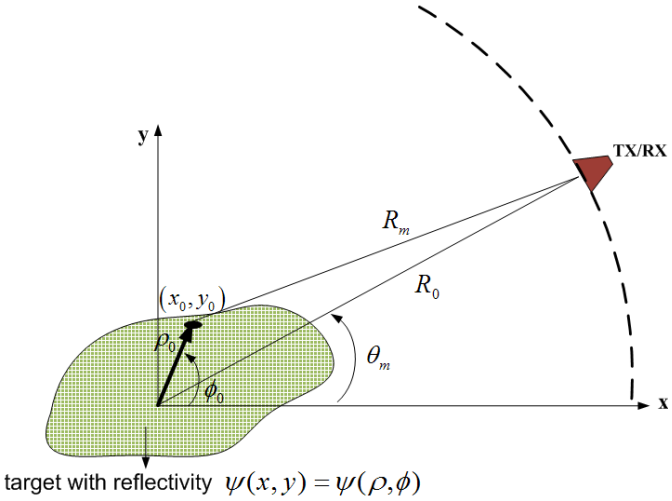

Figure 1. 2D monostatic imaging geometry for circular scanning.

circle of radius R_0 transmits stepped-frequency waveforms at the uniform samples of the azimuth angle positions θ_m. The illuminated target is considered to be composed of a number of independent point scatterers that are proportional to the scatterer reflectivity function ψ provided that the antenna's gain pattern is the same for all aspect measurement points of cylindrical configuration. Therefore, antenna's gain pattern is suppressed in the received field data. The projections of ψ onto the Cartesian and cylindrical coordinate image planes are denoted as $\psi(x, y)$ and $\psi(\rho, \phi)$, respectively. Assuming that ψ is independent from aspect and frequency, the measured scattering parameter measured at a specific angle θ_m for a point scatterer located at (x_0, y_0) or (ρ_0, ϕ_0) can be expressed as

$$S_{\theta_m}(k_r) = \psi(\rho_0, \phi_0) \frac{1}{R_m^2} \exp(-jk_r R_m) \tag{1}$$

where k_r is the radial spatial frequency (wavenumber) defined for the two-way propagation as $k_r = 4\pi f/c$, and R_m is the range from the antenna location to the scatterer. The total scattering can then be found by integrating all the responses due to each scatterers under the weak-scattering and uniform illumination assumptions, which yields

$$S_{\theta_m}(k_r) = \int_0^{2\pi} \int_0^{\infty} \frac{1}{R_m^2} \psi(\rho, \phi) \exp(-jk_r R_m) \rho d\rho d\phi \tag{2}$$

For a non-uniform illumination, antenna's gain pattern should also be included in Eq. (2) as an amplitude weight.

2.1. Focusing Operator Based Imaging

To obtain a reflectivity image of the target, an integral resembling inverse transform can be applied to the collected 2D data $S(k_r, \theta_m)$ with respect to k_r and θ_m, expressed as [30]

$$\psi(\rho, \phi) = \int_0^{\infty} \int_0^{2\pi} S(k_r, \theta_m) \exp(jk_r R_m) R_m^2(\rho, \varnothing - \theta_m) k_r dk_r d\theta_m \quad (3)$$

where the range $R_m(\rho, \varnothing - \theta_m) = \sqrt{R_0^2 + \rho^2 - 2R_0\rho\cos(\varnothing - \theta_m)}$ is valid under the near-field conditions, and "$\exp(jk_r R_m)R_m^2 k_r$" is the focusing operator that compensates the amplitude and the phase variations along the wave propagation path. Thus, a cylindrical representation of the reflectivity ψ can be estimated by numerically evaluating the integral in Eq. (3) for each location in the image. The result can then be mapped onto the Cartesian coordinates by using 2D interpolation procedures. For a $N_\rho N_\phi$ image points and a $N_{k_r} N_{\theta_m}$ data matrix of frequency and angle samples, the computational cost of the method amounts to $O(N_\rho N_\phi N_{k_r} N_{\theta_m})$ excluding the computation time for interpolation. Since this technique is computationally inefficient due to lengthy numerical integration,we only use it to test the performances of other imaging algorithms in our concealed object detection problem.

2.2. Back-projection Based Imaging

Let's first consider the range profile of the target at a specific angle θ_m which can be obtained by applying 1D inverse Fourier transform (IFT) to the spatial frequency data of Eq. (2) as follows

$$s_{\theta_m}(r) \triangleq IFT\{S_{\theta_m}(k_r)\} = \int_{-\infty}^{\infty} \int_{-\infty}^{\infty} \frac{1}{R_m^2} \psi(x, y) \delta(R_m - r) dx dy \quad (4)$$

Eq. (4) is known as the circular Radon transform of the target's reflectivity function which physically explains that the received signal for a spherical wavefront radiation is actually an average (integral) of the planar reflectivity function along the arc of a circle with a radius r. Thus, obtaining an image of the reflectivity can be thought as the process of inverting this circular averaging operation. One approach for this task is to use the back-projection algorithm that employs the *projection-slice theorem* for inversion [31, 32]. Basically, the theorem for the 2D space states that 1D Fourier transform (FT) of the range profile at an angle θ represents the slice of the 2D FT of the target's reflectivity at the same angle [33]. Hence, denoting the 2D FT of the reflectivity by $\Psi(k_x, k_y)$, the theorem proves that $S_\theta(k_r)$ should

be equal to $\Psi(k_r, \theta)$. In other words, the sampled representations of $\Psi(k_x, k_y)$ can be obtained from the FT of the projections $S_\theta(k_r)$ measured at various azimuth aspects.

The derivation of the back-projection algorithm begins with considering the IFT expression of the reflectivity function $\psi(x, y)$ given in Cartesian coordinates as follows

$$\psi(x,y) = \int_{-\infty}^{\infty}\int_{-\infty}^{\infty} \Psi(k_x,k_y)\exp\left[j\left(k_x x + k_y y\right)\right] dk_x dk_y \tag{5}$$

This equation can be modified to be written in the data collection coordinates (k_r, θ_m) as follows

$$\psi(x,y) = \int_{-\pi}^{\pi}\int_{0}^{\infty} \Psi(k_r,\theta_m)\exp\left(jk_r R_m\right) k_r dk_r d\theta_m \tag{6}$$

Using the principle of projection-slice theorem, Eq. (6) takes the form of

$$\psi(x,y) = \int_{-\pi}^{\pi}\left[\int_{0}^{\infty} S_{\theta_m}(k_r)\exp\left(jk_r R_m\right) k_r dk_r\right] d\theta_m \tag{7}$$

The bracketed integral in Eq. (7) can be regarded as the 1D IFT of a function $Q_{\theta_m}(k_r) = S_{\theta_m}(k_r)k_r$ evaluated at a specified R_m. Defining $q_{\theta_m}(r)$ as the IFT of this function, Eq. (7) can be represented as

$$\psi(x,y) = \int_{-\pi}^{\pi} q_{\theta_m}(R_m) d\theta_m \tag{8}$$

Eq. (8) is the final result of the back-projection algorithm which can be implemented for a stepped frequency waveform (SFW) transmission with the following steps:

Step 1: Pre-allocate an image matrix of zeros $\psi(x, y)$ to hold the values of the target reflectivity.

Step 2: Multiply the acquired spatial frequency data $S_{\theta_m}(k_r)$ with k_r.

Step 3: Take 1D IFT of the result to obtain $q_{\theta_m}(r)$ which represents the filtered version of the range profile $s_{\theta_m}(r)$.

Step 4: Calculate the R_m values of the each pixel location in the image and obtain its "$R_m^2 q_{\theta_m}(R_m)$" value through any interpolation scheme.

Step 5: Add interpolated values to $\psi(x, y)$.

Step 6: Repeat steps 2 thru 5 for the other observation angles θ_m.

In this implementation, a zero padding operation can also be applied to the collected spatial frequency data $S_{\theta_m}(k_r)$ to facilitate the subsequent interpolation step in the range domain. Neglecting the operations for the generation of range profiles and interpolation process, the numerical complexity of the back-projection algorithm is found as $O(N_x N_y N_{\theta_m})$ with N_{θ_m} being the number of angle points and N_x, N_y being the number of image points in x and y direction, respectively. Comparing with the focusing operator based algorithm, it is seen that the back-projection possesses N_f times lower operation with N_f being the number of frequency sample points. This is due to the fact that in the back-projection algorithm, each measured 1D data $(1 \times N_f)$ of range profiles are back-projected onto the imaging area in a block-wise manner. Hence, it allows a vector-based processing of measured data whereas an element-wise processing is performed in the focusing operator based algorithm.

2.3. Sampling Requirements

The collection of backscattering data should also be taken into consideration for an effective imaging. Under the SFW radar operation, the acquired data will give the frequency and angular domain samples of the backscattering signal. To avoid the loss of information in the reconstructed image, the sampling intervals used in these measurement directions of frequency f and azimuth angle θ should satisfy the Nyquist sampling criterion. Hence, the maximum allowable sampling interval in one domain can be determined by the extent in the transform domain. Assuming the target is confined within a hypothetical cylinder of radius $\rho_{\max}$, the sampling constraints for each measurement direction can then be calculated as explained in the following: As k_r being the radial spatial frequency for the two-way propagation as previously defined, the frequency step constraint needed to fulfill the Nyquist criterion can be calculated as

$$\Delta k_r \leq \frac{2\pi}{R_{\max}} \quad \text{or} \quad \Delta f \leq \frac{c}{2R_{\max}} \tag{9}$$

where Δk_r is the radial spatial frequency step, $R_{\max}$ is the spatial bandwidth of the observed distance in radial direction and Δf is the frequency step.

To determine the maximum angular step for an alias-free reconstruction, let us first obtain the instantaneous angular spatial frequency of the signal $S_{\theta_m}(k_r)$ given in Eq. (2) via

$$k_{\theta_m} = \frac{\partial}{\partial \theta_m} \left\{ \arg \left[S_{\theta_m}(k_r) \right] \right\} = \frac{k_r R_0 \rho \sin(\varnothing - \theta_m)}{\sqrt{R_0^2 + \rho^2 - 2R_0 \rho \cos(\varnothing - \theta_m)}} \tag{10}$$

Assuming that the target has an isotropic scattering over the 360° extent, the maximum and minimum values of k_{θ_m} occurs at

$$\begin{aligned} \theta_m|_{k_{\theta_m}\,\max} &= \varnothing - \cos^{-1}(\rho/R_0) \\ \theta_m|_{k_{\theta_m}\,\min} &= \varnothing + \cos^{-1}(\rho/R_0) \end{aligned} \tag{11}$$

which yields a spectral bandwidth of

$$BW_{k_{\theta_m}} = (k_{\theta_m\,\max} - k_{\theta_m\,\min}) = 2k_r\rho \tag{12}$$

This bandwidth has its maximum value for $f = f_{\max}$ and $\rho = \rho_{\max}$. Hence,the angular resolution step satisfying the Nyquist criterion for this worst case condition can be determined as

$$\Delta\theta_m \leq \frac{2\pi}{BW_{k_{\theta_m}}\big|_{f=f_{\max},\rho=\rho_{\max}}} = \frac{2\pi}{2k_{r\,\max}\rho_{\max}} = \frac{\lambda_{\min}}{4\rho_{\max}} \tag{13}$$

Comparing the results given in Eq. (9) and Eq. (13), it is important to note that although the frequency step is solely depending on the target size, the angular step should be decreased when the operating frequency is increased.

2.4. Resolutions

Based on the basic Fourier analysis, the spatial resolutions in the resulting 2D reflectivity images are determined by the extent of the data support region in the spatial frequency domain. Hence, they depend on the frequency bandwidth, the center frequency and the extent of the synthetic aperture. Besides, the traditional resolution formulas are usually defined according to a separable 2D coordinate system assuming that the support region is nearly in rectangular shape. These formulas, however, lose their validity for wide-angle data collections in which the range and cross-range resolutions are not essentially independent. In that case, the image resolutions should be deduced by approximations. One simple approach for predicting these resolutions is given in [34] that is based on the numerical calculation of the point spread function (PSF). The approach can be explained as follows:

i. Obtain and normalize the amplitude of the PSF image for an appropriate set of (k_r, θ_m) values.
ii. Determine the number of pixels exceeding the desired resolution threshold value of say -4 dB.
iii. Multiply the number of pixels by the single pixel area.

The result will then give the resolution cell area (RCA) of the image which can be used as a metric for the resolution calculation.

2.5. Calibration Procedure

Calibration should be done to account for the delay time of the measurement set-up and unwanted echo signal as well as to compensate all the losses inherent to the radar, transmission waveguides and antennas.The calibration procedure adapted in this paper involves the background subtraction process which can be implemented through the following steps:

i. Referring to the geometry given in Fig. 1, place a metallic sphere at the origin of the imaging coordinates and measure the far-field scattering data of the sphere $S_{sph}(f)$ for an arbitrary azimuth aspect angle. This reference signal can be assumed as constant for all the other measurement angles due to the sphere's rotationally symmetric backscattering feature.

ii. Measure the backscattered data of the background $S_{bck}(f)$ and the target $S_{tar}(f)$ for each viewing angle and obtain the corresponding complex I/Q data $S(f)$ given by

$$S\left(f\right) = \frac{S_{tar}\left(f\right) - S_{bck}\left(f\right)}{S_{sph}\left(f\right) - S_{bck}\left(f\right)} S_{sph}^{ana}\left(f\right) \tag{14}$$

where $S_{sph}^{ana}(f)$ denotes the analytical solution for the backscattering amplitude of the sphere. The acquired calibrated data $S(f)$ should also be multiplied by $\exp(jk_rR_0)$ to shift the origin of the range axis to the antenna location as assumed in the formulations of the imaging algorithms given in Subsections 2.1 and 2.2.

3. IMAGING RESULTS

3.1. Point Spread Function (PSF)

PSF of an imaging system is the image produced by applying a reconstruction algorithm to the return of a single point scatterer located at the origin of the coordinate system. PSFs can be used in evaluating the resolution and sidelobe metrics of the images resulting from the different data collection geometries, radar parameters and processing algorithms [35]. For this purpose, the PSFs of the MMW imaging system were examined for two different data collections that were considered in the conducted experiments of our study.

For the first collection, an angular span of $\theta = 0^\circ$ to 360° with 361 sampling points and a frequency range of $f = 80$ to 100 GHz with 256 sampling points were assumed. The distance of the monostatic antenna from the origin was selected as 1.3 m and the maximum radius of the imaging area was set to 4 cm by considering the sampling constraints

given in Subsection 2.3. The results for the focusing operator based and the back-projection based imaging algorithms are shown in Figs. 2(a) and 2(b), respectively. Comparing the figures, the sidelobe levels of the two images are shown to be nearly identical. As a quantitative analysis of the resolutions, the procedure explained in Subsection 2.4 was applied and the -4 dB RCAs of the images given in Figs. 2(a) and 2(b) were found to be equal to 0.3936 mm^2.

For the second situation, an angular span of $\theta = 0^\circ$ to 360° with 1441 sampling points and a frequency range of $f = 80$ to 90 GHz with 256 sampling points were considered. The antenna distance was again chosen as 1.3 m. To avoid aliasing, the maximum radius of the imaging area $\rho_{\max}$ was calculated according to Eq. (13) and found as $\rho_{\max} = \lambda_{\min}/(4 \times \Delta\theta) = 0.19$ m. The resulted PSF images for the two algorithms are shown in Fig. 3. When the images are visually compared, it is recognized that the back-projection algorithm yields relatively less sidelobe amplitudes mainly due to the zero-padding operation of the collected spatial-frequency data. Furthermore, the RCAs of the focusing operator and the back-projection results were calculated to be 78.73 and 9.84 mm^2, respectively. This resolution difference can be attributed to the fact that the 2D reformatting procedure of the focusing operator technique produces various levels of noise which in turn results in a poor resolution image. Hence, the back-projection processing provides also better resolved images for this particular data collection.

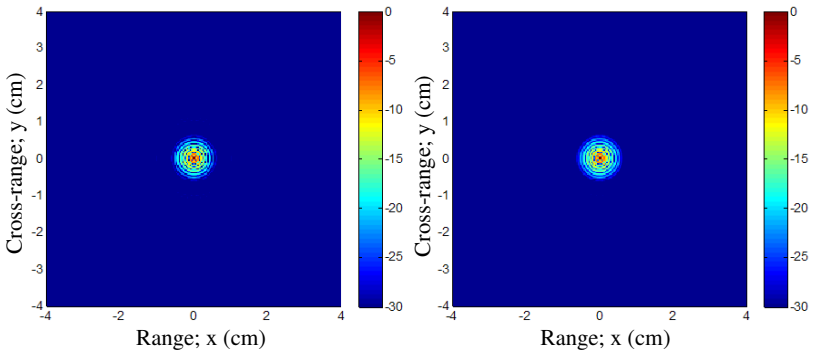

Figure 2. PSF images for an angular span of $0^\circ \sim 360^\circ$ with 361 sampling points and a frequency span of 80 $\sim$ 100 GHz with 256 sampling points: (a) Focusing operator, (b) back-projection based imaging.

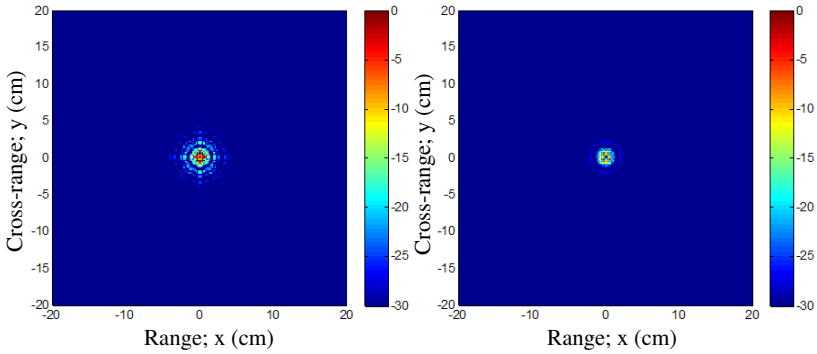

Figure 3. PSF images for an angular span of $0° \sim 360°$ with 1441 sampling points and a frequency span of $80 \sim 90$ GHz with 256 sampling points: (a) Focusing operator, (b) back-projection based imaging.

3.2. Experimental Results

The following experiments were conducted within the anechoic chamber of the *International Laboratory for High Technologies* (*ILHT*) at *Scientific and Research Council of Turkey-Marmara Research Center(TUBITAK-MRC)*. The circular scanning geometry of Fig. 1 was equivalently realized by rotating the targets placed on a turn table. Therefore, the geometry provides ISAR set-up. In all measurements, two circular horn antennas were used in a quasi-monostatic configuration and the distance of the midpoint of the antennas to the coordinate origin was kept fixed at a value of 1.3 m. Additionally, all collected data were calibrated according to the procedure explained in Subsection 2.4 and imaged by an application of both focusing operator and back-projection based algorithms for comparison reasons.

3.2.1. Experiment 1: Imaging Cube Targets

The objective of this experiment was to test the capabilities and limitations of the MMW imaging for various kinds and sizes of the cube target concealed underneath different fabric types. The selected targets were to be the $2\,\text{cm}^3$ metal cube, the $1\,\text{cm}^3$ metal cube and the $1\,\text{cm}^3$ teflon cube with a dielectric constant of 2.1. Two different types of fabrics; one being the 100% cotton (will be denoted by COTT afterwards) and one being the 100% polyester (will be denoted

by POLY from now on) were used during the measurements. The measured electric permittivities of these fabrics are listed in Table 1.

A series of measurements were then carried out for various target-fabric combinations as listed in the scenarios at Table 2. The frequency range was altered from 80 to 100 GHz and the angular span was chosen from 0° to 360° throughout the measurements. Taking the target encircling radius as $\sqrt{2}$ cm, the corresponding frequency/aspect sampling requirements were calculated according to Eqs. (9) and (13) such that the minimum numbers of frequency and angle measurements were found to be $N_f \geq 176$ and $N_\theta \geq 119$, respectively. Based on these calculations, the number of frequency and aspect sampling points employed in the experiment was chosen to be $N_f = 256$ and $N_\theta = 361$, respectively. Previous PSF results of this data collection provide the RCAs of the reconstructed images to be predicted around 0.3936 mm^2.

Figure 4 shows the imaging results of the 2 cm^3 metal cube for the fabric cases listed in Scenario 1 of Table 1. To evaluate the

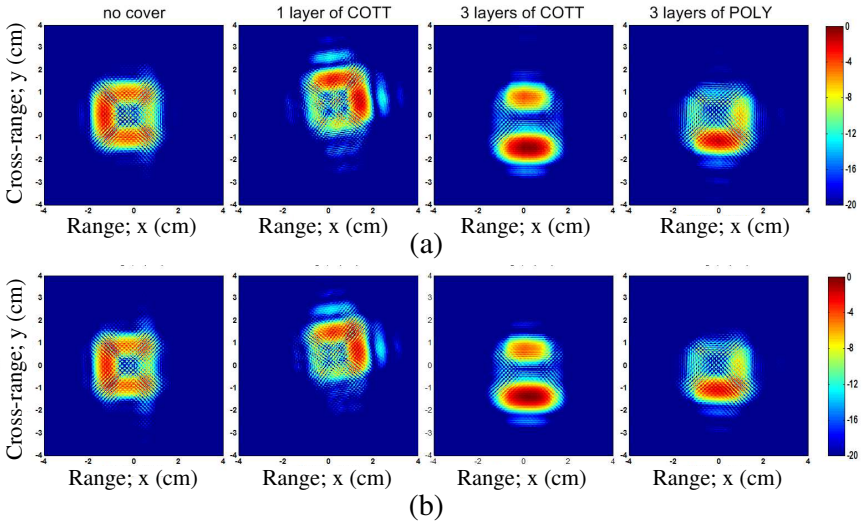

Figure 4. MMW radar images of the 2 cm^3 metal cube for different coverings: (a) Focusing operator, (b) back-projection based imaging.

Table 1. Properties of the cover materials used in the Experiment 1.

Material	*Structure*	*Measured electricpermittivity (F/m)*
COTT	100% cotton	$1.6859 \times \left(8.85 \times 10^{-12}\right)$
POLY	100% polyester	$1.2451 \times \left(8.85 \times 10^{-12}\right)$

Table 2. Targets and coverings used in the measurements of Experiment 1.

Scenario	*Target*	*Covering*
1	metal cube ($2\,\mathrm{cm}^3$)	no cover
		1 layer of $COTT$
		3 layers of $COTT$
		3 layers of $POLY$
2	metal cube ($1\,\mathrm{cm}^3$)	no cover
		1 layer of $COTT$
		1 layer of $POLY$
		3 layers of $POLY$
3	teflon cube ($1\,\mathrm{cm}^3$)	no cover
		1 layer of $COTT$
		1 layer of $POLY$
		3 layers of $POLY$

image reconstruction performance, both the focusing operator and the back-projection based imaging results are given in Figs. 4(a) and (b), respectively. When these results are visually compared, it is clearly seen that both algorithms yield very similar images of target reflectivity. To evaluate the MMW detection performance, the row images given in either Fig. 4(a) or 4(b) can be examined to reveal the following observations:

i. The cube is easily identified in its true shape and size for the "no cover" case. The subsequent images show some minor or major degradation with respect to this reference image.

ii. Comparing the image for "3 layers of $COTT$" with the image for "1 layer of $COTT$", it is shown that the thickness of the fabric adversely affects the success of detection, as expected.

iii. It is shown from the images for "3 layers of $COTT$" and "3 layers of $POLY$" that the $POLY$ result has less degradation than $COTT$ result although the thickness of the fabrics are the same in both cases.This asserts that detection through higher electric permittivity materials (i.e., $COTT$) is more difficult than that of lower permittivity (i.e., $POLY$) materials.

It is also worth noting that targets with flat surfaces such as the current cube targets reflect dominant energy when their surfaces are normal to the illumination direction. The results demonstrate that detection

of such targets becomes more difficult especially when this mechanism is altered through the usage of dielectric fabrics with low transmission properties. It is also beneficial to note that the center of the cube in the images for "1 layer of COTT" is shown to be displaced from the imaging center and also to have a different orientation with respect to other measurements. This is one example of our positioning errors which may be encountered also within the images of the subsequent measurements. In those cases, the cube was slightly moved and/or rotated from its true position when a covering layer was put on. This displacement however, does not constitute any problem to our detection task since the scattering data of our measurements cover an angular aperture of 360° thereby being independent from the target's orientation.

The results for Scenario 2 measurements of the $1\,\mathrm{cm}^3$ metal cube are obtained as shown in Fig. 5. As observed from Figs. 5(a) and 5(b), both imaging algorithms yield similar images again. To characterize the effects of different covering cases, the image for the "no cover" case is taken as the reference wherein the shape and size of the cube is clearly identified. It is readily recognized that there are a lot of discrepancies between this reference image and the image for "1 layer of *COTT*". This is again due to the relatively high electric permittivity of the *COTT* material. On the other hand, the images for "1 layer of *POLY*" and "3 layers of *POLY*" result in relatively good agreement

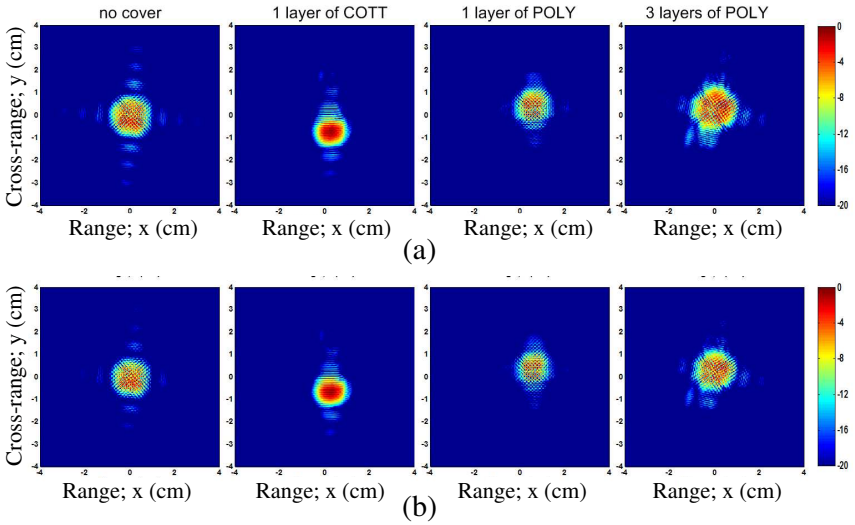

Figure 5. MMW radar images of the $1\,\mathrm{cm}^3$ metal cube for different coverings: (a) Focusing operator, (b) back-projection based imaging.

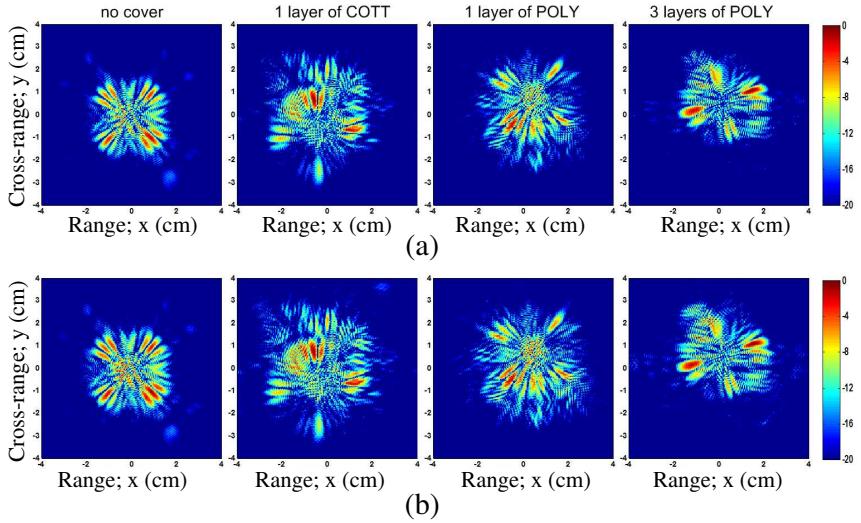

Figure 6. MMW radar images of the 1 cm^3 teflon cube for different coverings: (a) Focusing operator, (b) back-projection based imaging.

with the reference image which again demonstrates that as covering gets thicker, the detection tends to be more difficult.

The imaging results of the 1 cm^3 teflon cube for the Scenario 3 coverings are shown in Fig. 6. Both imaging algorithms produce nearly identical images again as depicted in Figs. 6(a) and 6(b). It is observed from these images that the reflected energy is dispersed through the azimuth angles and the exact shape of the cube is not truly obtained. For the "no cover" case; however, this dispersion is seen to be concentrated at the corners of the cube in a uniform reflection pattern. This regularity of the reflection can also be somewhat observed in the images for "1 layer of *POLY*" since this covering combination provides relatively good transmission of the electromagnetic wave. But, this reflection mechanism is seen to be considerably different for the other coverings of "1 layer of *COTT*" and "3 layers of *POLY*" whose images show random scattering features. From these results, it can be concluded that although small dielectric objects can be detected even underneath thick clothes, it may not be generally possible to infer their shapes from the resultant MMW images.

3.2.2. Experiment 2: Imaging a Handgun

In this experiment, a metallic handgun was used to test the imaging system performance of a real threatening target for different covering

situations as listed in Table 3. In addition to the *COTT* and *POLY* covers, *a winter coat* (%70 cotton and %30 polyester) was also utilized in this experiment. Fig. 7 shows some photographs of the measurement set-up and the handgun under this winter coat. Assuming the object can be confined into a circle with a radius of 19 cm and considering the sampling requirements, a frequency span of 80 GHz to 90 GHz with 256 stepped frequencies and an angular span of 0° to 360° with 1441 discrete measurement points were used throughout the experiment. From the previous PSF analysis for this data collection, the RCAs for the focusing operator and back-projection based reconstruction were expected to be 78.73 and 9.84 mm^2, respectively.

The imaging results for corresponding covering situation are shown in Fig. 8. Comparing the focusing-operator results given in Fig. 8(a) with the back-projection results given in Fig. 8(b), the gun's overall shape and dominant scattering features are more clearly displayed via the latter images. Thus, the back-projection

Table 3. Target and coverings used in the measurements of Experiment 2.

Target	*Covering*
handgun	no cover
	2 layers of *COTT*
	2 layers of *POLY*
	winter coat

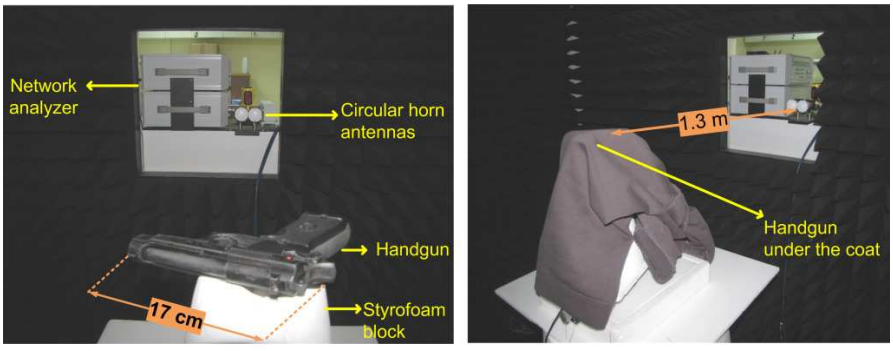

(a) (b)

Figure 7. Photographs from the second experiment: (a) Measurement set-up and the gun target, (b) gun covered with the winter coat.

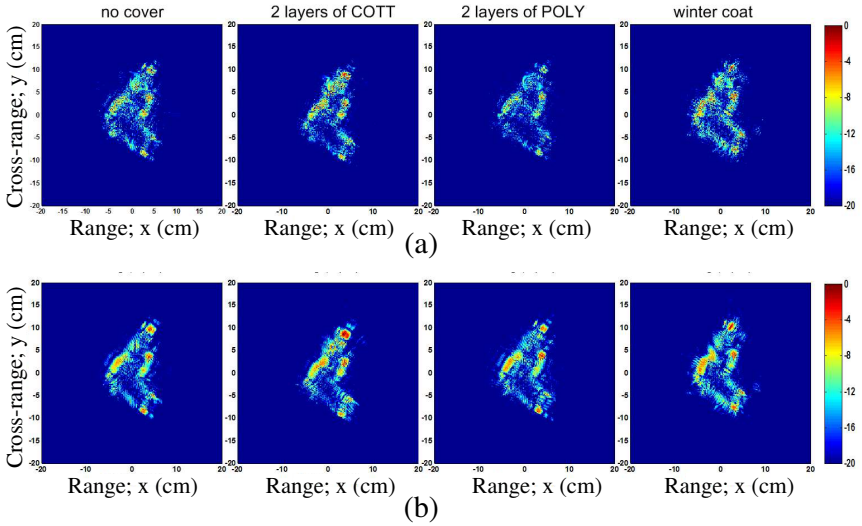

Figure 8. MMW radar images of the gun target for different coverings: (a) Focusing operator, (b) back-projection based imaging.

has produced, in this case, better quality images than the focusing-operator based reconstruction in terms of the resolution and the quality of scattering centers. This visual interpretation is also consistent with the estimated RCA values of these algorithms. Yet, each imaging result given in Fig. 8 is shown to be sufficient to effectively detect and identify the handgun for the investigated covering situation. Besides, a minor degradation is recognizable in the images of the handgun for the winter coat case; demonstrating the fact that the coarseness of the clothing may limit the reliable identification of threat objects.

4. CONCLUSION

In this work, the concealed object detection problem was investigated through MMW 2D imaging experiments conducted within an anechoic chamber. To test the high penetration and high resolution ability of MMW imaging, the wide-band monostatic backscattering data from various types of targets concealed under different textile fabrics were collected with the help of an ISAR scanning set-up. The sampling requirements for the full aperture data collection geometry and the calibration process were both treated carefully to be able to obtain a successful image. A modified near-field back-projection imaging algorithm was used to reconstruct the images. The results of a straightforward reconstruction algorithm called the focusing operator

based technique were also provided to characterize and compare the performance of the chosen algorithm.

The obtained results have shown to demonstrate the capability of the MMW imaging in producing the high resolution and efficient images of *metallic* small cube ($1\,\mathrm{cm}^3$ and $2\,\mathrm{cm}^3$) and a handgun targets under different kinds of clothing. From the results, it was observed that the size of these metallic objects and the structural properties (i.e., electric permittivity) and the coarseness of the corresponding coverings all have an influence on the successful detection. Furthermore, the detection becomes more difficult when the size of the investigated target gets smaller. The detection performance is also shown to be inversely proportional with the thickness and the electric permittivity value of the camouflage material.

On the other hand, the images of a *dielectric* small cube ($1\,\mathrm{cm}^3$) target under a cover material of moderate complexity (i.e., low electric permittivity) showed that it may be difficult to retrieve the exact shapes of this kind of objects by using the MMW band imagery. Besides, it was shown that their detection can be still achievable from the difference of contrast that is clearly visible in the produced images.

Finally, the results showed that, the back-projection algorithm that can be applicable to arbitrary data collection geometry is able to produce effective imaging of the concealed objects. Hence, the algorithm may be used as an alternative imaging technique to the RMA for bistatic data collections wherein the implementation of the widely utilized RMA becomes very difficult.

REFERENCES

1. Appleby, R. and R. N. Anderton, "Millimeter-wave and submillimeter-wave imaging for security and surveillance," *Proc. IEEE*, Vol. 95, No. 8, 1683–1690, Aug. 2007.
2. Appleby, R., D. A. Wikner, R. Trebits, and J. L. Kurtz, "Mechanically scanned real-time passive millimeter-wave imaging at 94 GHz," *Proc. SPIE*, Vol. 5077, 1–6, 2003.
3. The Autonomous Approach Landing Capability, http://www.baesystems.com/BAEProd/groups/public/documents/bae_publication/bae_pdf_eis_autonomous.pdf.
4. Navtech W800 Traffic Sensor, http://www.navtechradar.com/Documents/Highways/W800-Traffic%20both-nav%20rad.pdf.
5. Fetterman, M. R., J. Grata, G. Jubic, W. L. Kiser, Jr., and A. Visnansky, "Simulation, acquisition and analysis of passive

millimeter-wave images in remote sensing applications," *Optics Express*, Vol. 16, No. 25, 20503–20515, 2008.

6. Hua-Mei, C., L. Seungsin, R. M. Rao, M. A. Slamani, and P. K. Varshney, "Imaging for concealed weapon detection: A tutorial overview of development in imaging sensors and processing," *IEEE Signal Processing Magazine*, Vol. 22, No. 2, 52–61, 2005.
7. Oka, S., H. Togo, N. Kukutsu, and T. Nagatsuma, "Latest trends in millimeter-wave imaging technology," *Progress In Electromagnetics Research Letters*, Vol. 1, 197–204, 2008.
8. Gumbmann, F., P. Tran, A. Cenanovic, and S. Methfessel, "Millimeter-wave imaging concepts: Synthetic aperture radar (SAR) and digital beam forming (DBF)," *Frequenz*, Vol. 63, No. 5–6, 106–110, 2009.
9. Yeom, S., D. Lee, J. Son, M. Jung, Y. Jang, S. Jung, and S. Lee, "Real-time outdoor concealed object detection with passive millimeter wave imaging," *Optics Express*, Vol. 19, No. 3, 2530–2536, 2011.
10. Sato, H., K. Sawaya, K. Mizuno, J. Uemura, M. Takeda, J. Takahashi, K. Yamada, K. Morichika, T. Hasegawa, H. Hirai, H. Niikura, T. Matsuzaki, S. Kato, and J. Nakada, "Passive millimeter-wave imaging for security and safety applications," *Proc. SPIE*, 76720, 2010.
11. Essen, H., H. Fuchs, M. Hagelen, S. Stanko, D. Notel, S. Erukulla, J. Huck, M. Schlechtweg, and A. Tessmann, "Concealed weapon detection with active and passive millimeter-wave sensors, two approaches," *German Microwave Conference*, Karlsruhe, Germany, Mar. 2006.
12. Yeom, S., D. Lee, H. Lee, J. Son, and V. P. Gushin, "Distance estimation of concealed objects with stereoscopic passive millimeter-wave imaging," *Progress In Electromagnetics Research*, Vol. 115, 399–407, 2011.
13. Grossman, E. N. and A. J. Miller, "Active millimeter-wave imaging for concealed weapons detection," *Proc. SPIE, Conference of Passive Millimeter-Wave Imaging Technology VI and Radar Sensor Technology VII*, Vol. 5077, 62–70, 2003.
14. Jaeger, I., L. Zhang, J. Stiens, H. Sahli, and R. Vounckx, "Millimeter wave inspection of concealed objects," *Microwave and Optical Technology Letters*, Vol. 49, No. 11, 2733–2737, 2007.
15. Tan, W., W. Hong, Y. Wang, and Y. Wu, "A novel spherical-wave three-dimensional imaging algorithm for microwave cylindrical scanning geometries," *Progress In Electromagnetics Research*,

Vol. 111, 43–70, 2011.

16. Manfred, H., B. Gunnar, and E. Helmut, "Millimetre wave near-field SAR scanner for concealed weapon detection," *Proceedings of EUSAR*, 151–154, Friedrichshafen, Germany, 2008.
17. Harmer, S. W., S. E. Cole, N. J. Bowring, N. D. Rezgui, and D. Andrews, "On body concealed weapon detection using a phased antenna array," *Progress In Electromagnetics Research*, Vol. 124, 187–210, 2012.
18. Qi, F., V. Tavakol, D. Schreurs, and B. K. J. C. Nauwelaers, "Limitations of approximations towards fourier optics for indoor active millimeter wave imaging systems," *Progress In Electromagnetics Research*, Vol. 109, 245–262, 2010.
19. Tan, W., W. Hong, Y. Wang, and Y. Wu, "A novel spherical-wave three-dimensional imaging algorithm for microwave cylindrical scanning geometries," *Progress In Electromagnetics Research*, Vol. 111, 43–70, 2011.
20. Li, S., B. Ren, H.-J. Sun, W. Hu, and X. Lv, "Modified wavenumber domain algorithm for three-dimensional millimeter-wave imaging," *Progress In Electromagnetics Research*, Vol. 124, 35–53, 2012.
21. Sheen, D. M., D. L. McMakin, and T. E. Hall, "Three-dimensional millimeter-wave imaging for concealed weapon detection," *IEEE Trans. on Microwave Theory and Techniques*, Vol. 49, No. 9, 1581–1592, Sep. 2001.
22. Zhang, L., "Millimetre wave imaging for concealed target detection," Ph.D. Thesis, University of London, 2011.
23. Detlefsen, J., A. Dallinger, S. Huber, and S. Schelkshorn, "Effective reconstruction approaches to millimeter-wave imaging of humans," *Proceedings of the URSI General Assembly*, New Delhi, India, Oct. 23–29, 2005.
24. Sheen, D. M., D. L. McMakin, and T. E. Hall, "Near-field three-dimensional radar imaging techniques and applications," *Applied Optics*, Vol. 49, No. 19, E83–E93, 2010.
25. Bertl, S., A. Dallinger, and J. Detlefsen, "Broadband circular interferometric millimetre-wave ISAR for threat detection," *Advances in Radio Science*, Vol. 5, 147–151, 2007.
26. Bertl, S., A. Dallinger, and J. Detlefsen, "Bistatic extension for coherent MMW-ISAR-imaging of objects and humans," *Advances in Radio Science*, Vol. 6, 63–66, 2008.
27. Bertl, S., A. Dallinger, and J. Detlefsen, "Interferometric focusing for the imaging of humans," *IET Radar Sonar & Navigation*,

Vol. 4, No. 3, 457–463, 2010.

28. Fortuny, J. and J. M. Lopez-Sanchez, "Extension of the 3-D range migration algorithm to cylindrical and spherical scanning geometries," *IEEE Trans. on Antennas and Propagation*, Vol. 49, No. 10, 1434–1444, 2001.
29. Qi, Y. L., W. Tan, Y. Wang, W. Hong, and Y. Wu, "3D bistatic omega-k imaging algorithm for near range microwave imaging systems with bistatic planar scanning geometry," *Progress In Electromagnetics Research*, Vol. 121, 409–431, 2011.
30. Broquetas, A., J. Palau, L. Jofre, and A. Cardama, "Spherical wave near-field imaging and radar cross-section measurement," *IEEE Trans. on Antennas and Propagation*, Vol. 46, No. 5, 730–735, 1998.
31. Munson, D. C., J. D. O'Brien, and W. K. Jenkins, "A tomographic formulation of spotlight-mode synthetic aperture radar," *Proc. IEEE*, Vol. 71, No. 8, 917–925, 1983.
32. Bauck, J. L. and W. K. Jenkins, "Tomographic processing of spotlight mode synthetic aperture radar signals with compensation for wavefront curvature," *International Conference on Acoustics, Speech, and Signal Processing, ICASSP-88*, Vol. 2, 1192–1195. 1988.
33. Mersereau, R. and A. Oppenheim, "Digital reconstruction of multidimensional signals from their projections," *Proc. IEEE*, Vol. 62, No. 10, 1319–1338, 1974.
34. Luminati, J. E., "Wide-angle multistatic synthetic aperture radar: Focused image formation and aliasing artifact mitigation," Ph.D. Thesis, Air Force Institute of Technology, Wright-Patterson Air Force Base, Ohio, USA, 2005.
35. Ozdemir, C., *Inverse Synthetic Aperture Radar Imaging With MATLAB Algorithms*, 156, Wiley-Interscience, 2012.